

UAV Icing: Numerical Simulation of Propeller Ice Accretion

Nicolas C. Müller* and Richard Hann †

Norwegian University of Science and Technology, Trondheim, State, 7014 Trondheim

Thorsten Lutz

University of Stuttgart, Institute of Aerodynamics and Gas Dynamics, Germany

In-flight icing on unmanned aerial vehicles is a severe hazard and imposes limits to the operational envelope. Icing has shown to lead to substantial aerodynamic performance losses on lifting surfaces and propellers. In this paper, a method to estimate the ice accretion on a propeller of a UAV using modern numerical methods is being developed. This method is used to calculate the ice shape in three different meteorological conditions. The results indicate, that the ice morphology had a strong influence on the aerodynamic properties of the rotor. All icing cases do increase the drag and therefore the power requirement of the rotor, which will limit the range of the UAV. While the performance penalties at temperatures closer to the freezing point are only small, the ice accretion can have a large impact on the thrust and the efficiency of a propeller. This paper highlights the need to implement proper procedures to avoid icing conditions in UAVs. If flying in icing conditions cannot be avoided, effective deicing or anti icing systems on the rotors of UAVs need to be implemented.

I. Introduction

The development of newer and smaller scale electronics and control system has led to increased usage of small fixed-wing unmanned aerial vehicles (UAVs) with a wingspan of 2 to 4 meters in many different applications. In their new roles, they face different weather hazards. One frequent weather condition is the in-flight icing [1]. In-flight icing occurs in meteorological conditions where supercooled liquid water exists in the atmosphere. When these supercooled droplets collide with the airframe, they freeze and accumulate over time. The resulting ice accretions can lead to severe aerodynamic performance penalties, especially on unmanned aircraft [2]. Manned aviation is facing the same hazard of in-flight icing [3], and extensive research has been done to understand and mitigate this issue. For UAVs, the first research has been conducted in the 1990s [4], making this a comparatively new and emerging research topic. Several studies have since been conducted to investigate the impact of icing on UAVs. The majority of these studies has been focused on the icing on the wings of UAVs, analysing the icing using numerical or experimental methods [5],[6], [7], [8]. The existing literature shows that ice has severe negative effects on lifting surfaces, typically leading to a decrease in lift, increase in drag, and reduction of stall angles. Only recently has the in-flight icing on UAV propellers been researched. Several experimental and numerical studies have shown that icing leads to a very rapid decrease in thrust and performance efficiency whereas torque is substantially increased [9], [10]. The literature suggests that propeller icing leads to faster and more severe performance penalties compared to icing on lifting surfaces. Therefore, propeller icing is a significant threat to UAV operations and deserves in-depth investigations.

The aim of this paper is to develop a process for the estimation of the the ice accretion on the propeller of a small-medium UAV under different meteorological conditions using ANSYS FENSAP-ICE. To archive this goal, a number of steps was performed:

- Find experimental data
- Conduct a grid dependency study
- Validate the performance simulation
- Validate the ice accretion simulation
- Run the propeller in three different icing cases
 - Ice accretion
 - Performance calculation
 - Anti-icing simulation

*PhD candidate, Centre for Autonomous Marine Operations and Systems, Department of Engineering Cybernetics, nicolacm@stud.ntnu.no

†Post-doc, Centre for Autonomous Marine Operations and Systems, Department of Engineering Cybernetics, and AIAA Member. richard.hann@ntnu.no

Then the results of the ice accretion simulations are discussed, and explanations for the phenomena is suggested. Furthermore, the paper helps to identify the most hazardous icing conditions which is an important design aspect for ice protection systems [11], [12].

II. Data basis and methods

A. Experimental data

The main focus of the icing research has been the manned aviation. So the focus of experimental campaigns has been on icing in higher Reynolds number conditions than what a typical UAV does experience [13]. Only a few years ago, the first larger scale experimental campaigns to analyze icing on UAVs has been conducted [13].

For icing on rotors, the main focus has been on the icing on propellers and rotors of helicopters. In the course of this paper, a database of icing experiments on aircraft and rotorcraft has been generated, which will be presented in the following chapters. Icing experiments can be divided according to the type of data they aim to generate. The categories are the impingement experiments, ice accretion experiments and the aerodynamic performance studies.

1. Impingement data

Impingement experiments are conducted at higher temperatures to prevent ice from forming, but rather aim to detect the amount of water that impinges the aircraft at different locations. To locate the amount of water, that impacts each region, special colored paper can be used to detect the water [14]. Most impingement data has been collected in the impingement on the wings of manned aircraft. No impingement study has been performed on the impingement on the propeller of a UAV.

2. Ice accretion data

Another type of icing experiment is an ice accretion study. Those experiments are conducted in an icing wind tunnel (IWT). A IWT is similar to a classical wind tunnel, with a cooling system to provide low air temperatures, and a spray system, which enables the injection of water droplets into the airflow before entering the testing chamber. Therefore, experiments at set temperatures, with a fixed LWC and MVD can be conducted. An example for a IWT is the Icing Research Tunnel at the Glenn Research Center of the NASA [15]. The final ice shape can be detected using manual tracings, or in more recent experiments 3D Scans of the ice are performed. The total mass of the ice on the test model can be measured.

3. Ice performance penalties

Due to the additional provisions for the water droplet spray systems, an IWT commonly can not be used for the measurement of the aerodynamic influence of icing. To measure the performance degradation, an artificial ice shape is produced, and then attached to the test model in a wind tunnel to measure the performance loss by this ice shape. This ice shapes can be derived from experiments, or from icing simulations.

4. Database

A database including all literature with experimental data (impingement, ice accretion, performance penalties). was created. For this database, existing experiments have been collected. The experiments eligible for the database had to be either impingement measurement or ice accretion studies or a study of the performance penalties. All experiment have to be either published. The experiments were classified according to the type of the study. Additionally the range of the used Reynolds numbers and Mach numbers was listed. For the ice accretion experiment the icing conditions are listed. The data created in the experiments is listed. Examples for the possible data types would be manual tracings or 3D scans. All experiments were separated into experiments that are quasi-2D or 3D experiments. In a quasi-2D experiment, the boundary conditions and the geometry are constant in one direction perpendicular to the airflow.

In total 71 publications with ice accretion have been collected and sorted into a database which has been published in [16]. This database can be used for the validation of the numerical calculations. For this, the experiments are recreated using numerical methods, and the results are compared to the results from the experiments.

In this paper, an experiment on the AERTS where the ice accretion investigated on a model of a helicopter blade using a NACA0012 airfoil was considered for the validation of the ice accretion simulation. In the Chapter IV, the

results of the ice accretion were compared to the results of the ice accretion study at the University of Iowa State university on the ice accretion on a propeller of a UAV. A shot overview over the two experiments is given in Table 1.

Title	Geometry	Year	Source
An experimental study on the transient ice accretion process over the blade surfaces of a rotating UAS propeller	UAV Propeller	2017	[17]
An experimental correlation between rotor test and wind tunnel ice shapes on NACA 0012 airfoils	Helicopter rotor	2017	[18]

Table 1 Experimental data used in this paper.

In this section the used method and the data basis for the paper are presented.

B. Propeller aerodynamics

The thrust of an airplane can be produced by a propeller. The angle at which the flow hits the airfoil of the propeller is dependent on the velocity of the aircraft and the rotational velocity. The advance ratio J describes the ratio of the velocity generated by the rotation n along the diameter d of the propeller, to the aircraft velocity v_∞ [19].

$$J = \frac{v_\infty}{n d} \quad (1)$$

The lift of the propeller will show a component in the direction of the rotational axis. This force is called the thrust T of the propeller. Because most propellers will be symmetrical along the axis of rotation, the forces radial to the axis of rotation will cancel with the same force generated by the other propeller blades. To compare propellers of different sizes and under different atmospheric conditions, the dimensionless thrust coefficient C_T is introduced. The thrust coefficient is dependent on the rotational speed n of the propeller, compared to the velocity of the aircraft. For this reason, the thrust coefficient is dependent on the advance ratio.

$$C_T = \frac{T}{\rho n^2 d^4} \quad (2)$$

Next to the thrust, the propeller will produce a momentum Q against the rotation of the propeller. This momentum is caused by the drag of the propeller blades, as well as the induced drag, which the blades produce when they spin. This momentum Q can be calculated by the coefficient C_Q according to Equation 3.

$$C_Q = \frac{Q}{\rho n^2 d^5} \quad (3)$$

To overcome this momentum, and maintain a constant rotation speed, a certain power is required. This power can be calculated from the momentum and the rotational speed. To compare different propellers, the power coefficient C_P is used according to Equation 4.

$$C_P = \frac{P}{\rho n^3 d^5} \quad (4)$$

If the advance ratio of the propeller is larger than zero, the efficiency of the propeller can be calculated by comparing the power input to the propeller to the mechanical power the propeller will generate.

C. Numerical model

For the numerical calculation of the icing, ANSYS FENSAP-ICE version 20.1 is used [20]. This provides a suite of different modules, to calculate the different aspects of the ice accretion process. ANSYS FENSAP-ICE consist of three different programs used for the icing simulation, which will all be presented in this part.

- FENSAP
- DROP3D
- ICE3D
- FLUENT Meshing

FENSAP is the fluid solver, DROP3D calculates the fluid particle trajectories, and ICE3D is the ice accretion solver. The simulation is an iterative process. In the beginning, FENSAP calculates the airflow. After FENSAP reaches a finished solution for the airflow in this step, DROP3D calculates the Droplets trajectories and ICE3D calculates the new ice shape. Afterwards the simulation is remeshed using Fluent meshing. This is necessary to enable FENSAP to calculate the flow taking into account the new ice shape. This loop is repeated for ten times in every icing simulation in this paper.

For the calculations of the performance degradation, the flowfield is calculated using FENSAP. It is first used to calculate the flowfield using the clean performance mesh of the simulation. After the icing simulation, a new mesh is generated in Pointwise, and FENSAP is then used to calculate the aerodynamic performance of this new mesh.

1. FENSAP

FENSAP is a state-of-the-art CFD solver. It is used for the ice accretion results, as well as the standalone aerodynamics simulations. FENSAP is applied to calculate a steady state airflow. It utilizes a weak Galerkin finite element method for the spatial resolution. FENSAP is used to calculate the flowfield by using the full Navier-Stokes equation to calculate a compressible airflow. The turbulence is modeled using RANS equations and a $k-\omega$ SST turbulence model for the performance calculations or a Spalart-Allmaras turbulence model for the icing simulations.

During the icing simulations, the flowfield calculated in FENSAP is used to calculate the droplet distribution, and the Shear stress values calculated by FENSAP are used to calculate the ice shape in ICE3D [20].

2. DROP3D

The droplet distribution is calculated using a Eulerian multiphase model using DROP3D. It takes the velocities of the flowfield and calculates the distribution [20]. It calculates the impingement data that is vital for the calculation of the ice shape [21].

3. ICE3D

The ICE3D module performs the calculation of the ice accretion rate. It takes the impingement values from DROP3D and the friction forces from FENSAP. It uses the Messiger model.

ICE3D is able to calculate the required loads of a icing protection system (IPS). For this estimation, it solves the equation for the heat flux in order to calculate the required load to keep the temperature of the propeller surface at 0°C. This would prevent any ice from forming. Here two different modes of IPS operation are distinguished. In the running wet scenario, the loads to keep the fluid film at 0°C are calculated, while in the fully evaporative simulation mode, the required loads for the evaporation of all the water that impacts the surface is calculated. The fully evaporative operation mode has the benefit, that no runback icing is possible [20].

4. Fluent meshing

After each cycle, a new volume mesh is created using Fluent meshing. For this, the ice shape calculated by ICE3D is extracted, and combined with the wind tunnel from the volume mesh [22]. To unite both geometries, a surface wrapping operation is performed. In this operation, beginning from a point which is known to be in the computational region, a mesh is calculated to cover the whole surface of the new geometry. The grid size of this mesh can be specified for each contacting surface. This new watertight mesh is used as a basis for the calculation of the new volume mesh. This new volume mesh has similar meshing settings to the initial mesh, in order to get similar results. After the new volume mesh has been calculated, the flow solution is interpolated from the old mesh to the new mesh, in order to accelerate the convergence in future meshing steps.

5. Rotation

The propeller is rotating through the computational domain. This needs to be captured in the simulation, as it is very important for the flow field through the propeller. There are many ways to capture the rotation of a object. The first option, is to rotate the geometry and create a new mesh with the new position of the propeller. After the new mesh has been generated, the solution could be interpolated on the new mesh, and a new time-step could be calculated. This is very inefficient, as for every time-step a new mesh has to be calculated, this option is not used. In ANSYS FENSAP, the rotation is calculated, by using a rotating reference system. In this case, the mesh stays the same, throughout the

simulation. The velocities are not calculated in reference to a stationary mesh, but the mesh does rotate around the assigned axis. All velocities are calculated in reference to this rotating mesh. For the post processing, the velocities transformed to a stationary mesh [20].

6. Interfaces

Because most propellers are rotational periodic, it is not necessary to calculate the full propeller. For the propeller with 2 blades, it is enough to calculate half of the propeller, and use a periodic interface condition to simulate the other half. In ANSYS FENSAP-ICE, conformal periodic interfaces are used. This means, that every node at the interface has a corresponding node at the other side of the Interface. All values are exchanged over the interface, as if the other side were a neighboring cell in the mesh. Only the velocity gets transformed. For this transformation, the velocity vector is rotated around the axis of rotation in the angle of the two interface boundary. In the case of the two bladed propeller, the rotation angle is 180°.

7. Post processing

The post processing is done in Tecplot 360 EX in the version 2019 R1. This program is used to calculate the forces of the propeller. For this the forces along the axis have to be calculated, as well as the moment along the axis of rotation. The first step is to calculate the normal vector \bar{n} of the mesh at the surface of the propeller. The derivative of the normal vector in each spatial direction are n_X , n_Y and n_Z . The derivative of the shear stress vector in each dimension are given by ANSYS FENSAP, and are τ_X , τ_Y and τ_Z . The pressure p and the reference pressure p_{Ref} are taken from ANSYS FENSAP and the setup of the simulation. With this information, for each face the forces in each direction can be calculated with Equations 5, 6 and 7.

$$f_X = \tau_X - n_X * (p - p_{Ref}) \quad (5)$$

$$f_Y = \tau_Y - n_Y * (p - p_{Ref}) \quad (6)$$

$$f_Z = \tau_Z - n_Z * (p - p_{Ref}) \quad (7)$$

The thrust can be derived by integrating the force in the direction of the propeller axis over the surface of the propeller. Because only one blade of the propeller is calculated, the force needs to be multiplied by the amount of blades in the propeller. The moment of the propeller can be calculated using the position of the face in a cartesian coordinate system in the center of the rotation.

D. Geometries

1. DA4002

The first validation case is the DA4002 propeller created by Deters [23]. This propeller was chosen for the availability of good data. This propeller uses a Clark-Y airfoil. The trailing-edge of the airfoil has been modified using XFOIL version 6.47 [24] to get a trailing-edge gap of 1 mm, with a blending distance of 80% of the chord length of the airfoil. The distribution of the twist and the chord of the propeller over the radius can be seen in Figure 2. The propeller blade has a constant chord length of 180mm. To construct the shape of the propeller, the cross section of the propeller has been calculated at 14 cross sections. The central hub of the propeller has been simulated as a cylinder, with a free shape to connect the hub to the first layer of the propeller. This has been performed using XFOIL.

To generate the geometry for the propeller, a Matlab script was generated, to generate a file with the position of the points on the airfoil at 13 cross sections of the propeller. This point cloud was imported into CATIA V5 [26], and the shape of the propeller was created by connecting the cross sections. The hub of the propeller was approximated using a cylindrical shape. The final shape of the propeller in the simulation can be seen in Figure 3.

The radius of the simulation region is 5 times as wide as the radius of the propeller, and the distance between the propeller and the inlet and outlet is 2.5 times the radius of the propeller. This is done to ensure that the boundary conditions have a minimal influence on the aerodynamic coefficients of the propeller. Only half of the propeller is simulated, the other half is simulated using conformal periodic interfaces. This reduces the amount of cells in the simulation by half. The final configuration of the simulation can be seen in Figure 4.

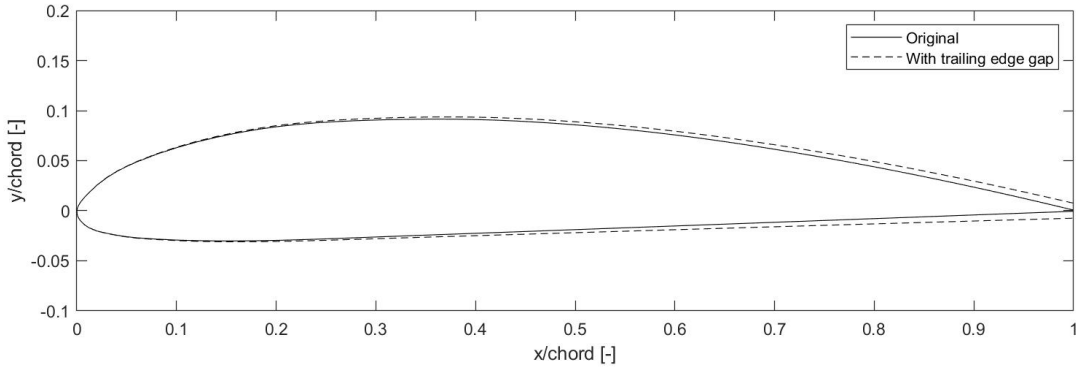


Fig. 1 ClarkY airfoil with and without trailing-edge gap [25].

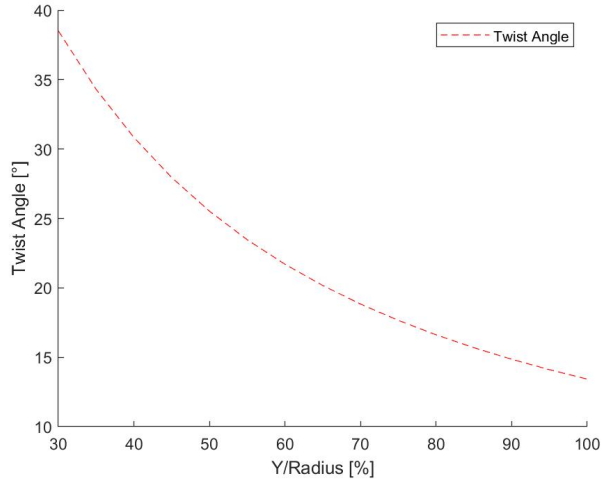


Fig. 2 Twist distribution of the DA4002 propeller [23].

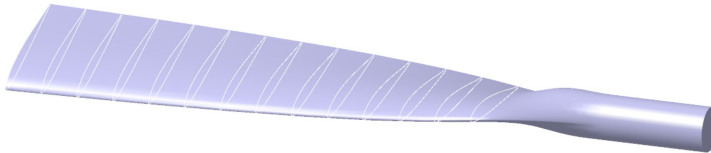


Fig. 3 Geometry of the DA4002 propeller with cross sections.

2. Simulation Setup

To simulate the airflow, a hybrid volume mesh was created using Pointwise. All grids consist of a structured prism mesh over the surface of the Propeller, and an unstructured tetrahedral Mesh in the farfield. The surface mesh on the propeller is a diagonalized structured mesh. Only the mesh in the front of the tip and the hub is an unstructured triagonal mesh. To estimate the influence of the grid on the simulation, a grid influence study has been performed. For this reason three grids have been created, with different amounts of grid refinements. The grids have a different amount of chordwise cells over the propeller. The settings for the different grids can be seen in Table 2.

For all grids the amount of cells on the farfield of the simulation was kept the same. This is the reason, why the amount of cells is not growing linear with the amount of chordwise cells.

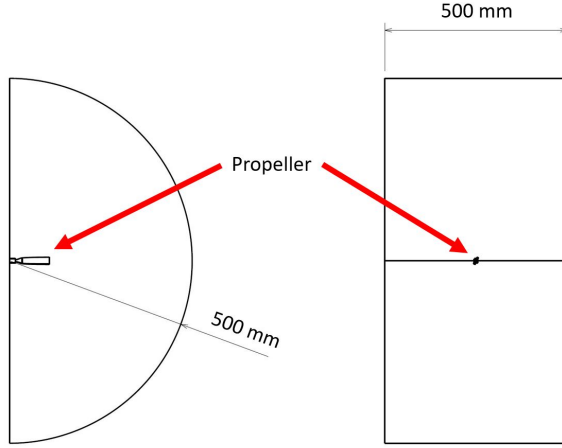


Fig. 4 DA4002 propeller in the wind tunnel.

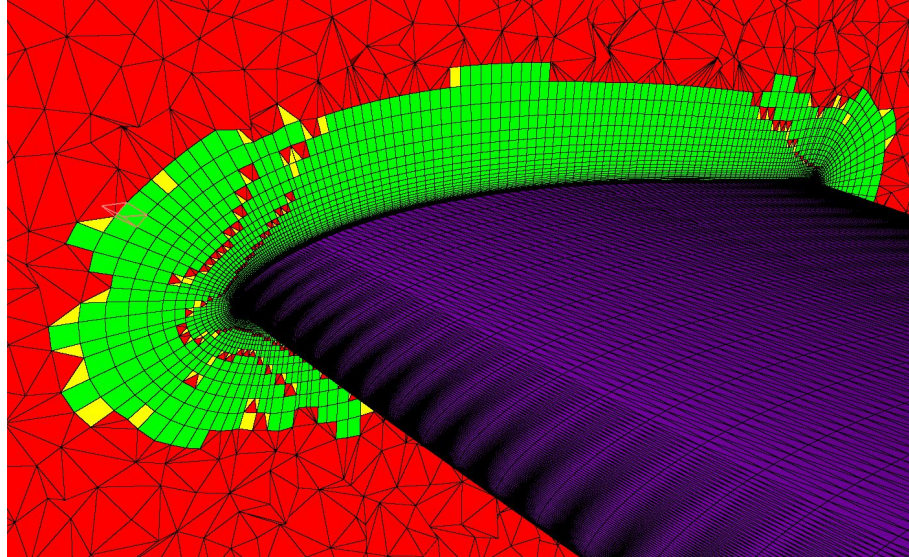


Fig. 5 Slice of the mesh of the DA4020 propeller.

3. NACA0012

To validate the ice accretion on a rotor, the ice accretion on a helicopter rotor with a NACA0012 airfoil was analysed. The rotor has a constant chord of 266 mm and a radius of 2.74m. The rotor was tested in a cylindrical testing chamber with a radius of 3m. The thickness of the trailing-edge was changed to a thickness of 1 mm in XFOIL.

4. Simulation Setup

For this simulation, the rotor was set in a round test chamber with a rectangular testing section. The outer wall represents the fixed outer wall of the test chamber. This testing chamber is stationary. The real test stand is 3.5 meter high, but because the pitch of the blade at the test is zero, no velocity along the axis of rotation is to be expected, so the height of the computational domain in this simulation is 1 meter.

The walls at the top and the bottom, as well as the center of the simulation are calculated as no slip walls. The outer wall and the rotor are set as standard walls. The ice accretion is only calculated on the rotor. The setup of the simulation can be seen in Figure 6 and Figure 7. The hub of the Propeller is not calculated. A cylinder with no-slip walls is used as a stand in for the hub of the propeller. The reason for this setup is the reduced number of cells in the simulation. The amount of cells on the wall of the propeller is very important for the amount of cells in the mesh, as it has the smallest

Parameter	Grid A	Grid B	Grid C
Spanwise cells	100	120	120
Chordwise cells	93	129	166
Prism Cells	2,116,871	3,215,833	3,947,038
Farfield Cells	4,247,629	5,369,395	5,775,871
Total Cells	6,364,500	8,585,228	9,722,909

Table 2 Grid refinement study on the DA4002 mesh.

cell sizes and prism layers. To calculate the rotation of the fluid, the air needs to be kept stationary in the simulation chamber. For this reason, in front of the propeller is a outlet, and behind the propeller, there is a outlet. The velocity of the inlet is set to 0 m/s in an absolute coordinate system. Another system would be to calculate the full chamber and to use the sides and top an bottom of the simulation for the momentum transfer into the air. This was not done, as this would require the full experimental chamber to be calculated. this would have lead to a cell count too large for the remesher, due to virtual memory constraints on the computational cluster. Furthermore does the experiment chamber have stationary surfaces, which are not tangential to the rotational velocity of the propeller. This surfaces cannot be calculated using the used method for the calculation of the rotation.

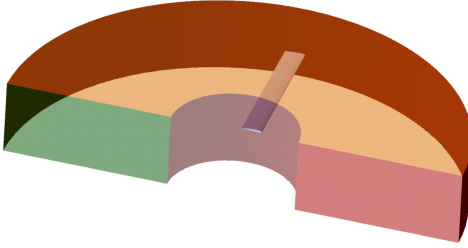


Fig. 6 Model of the NACA0012 in the simulation wind tunnel.

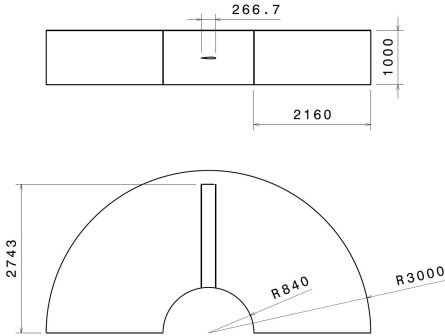


Fig. 7 Drawing of the simulation wind tunnel of the NACA0012 rotor.

For the icing simulation, the initial grid was created in Pointwise, and the volume is remeshed using ANSYS FLUENT. To enable the optimized mesh setup during the remeshing step, the surface of the propeller is split up into 6 boundaries. At the leading-edge of the rotor, two boundaries have been created, covering the first 10% of the chord of the airfoil. Because on the ice accretion is focused on this areas, the resolution for this regions is refined. An overview over the refinements on the mesh are given in Table 3.

5. Propeller

In this paper, the propeller of a medium sized UAV was analyzed. The UAV for which this propeller is intended, is the Maritime Robotics PX-31 Falk. It has a wing span of 3.2 meters, a cruise velocity of 25 m/s and can carry a payload of up to 7 kg [27]. The performance data for the PX-31 can be seen in Table 4. The PX-31 Falk is intended for long-range and surveillance missions. Those missions could include research in the Arctic, thus requiring the operation under adverse weather conditions including atmospheric icing.

We obtained a suitable comparable propeller for the PX-31, which was provided for us by Mejzlik. The propeller for this UAV has a diameter of 0.533 m and a pitch of 0.254 m. The name of the propeller is the 21x10 EL. The shape of the propeller can be seen in Figure 8.

To improve the mesh quality for the CFD calculations, the trailing-edge has been thickened to 0.5 mm using CATIA Version 5.19 [26]. The trailing-edge has been symmetrically extended, and at the blunt edge was blended during the last 80% of the chord of the propeller. In Figure 10 the airfoil of the propeller can be seen at 75% of the radius. The airfoil

Boundary	Boundary Condition	Max. Cell size [mm]
Leading-Edge Top	Wall	1
Leading-Edge Bottom	Wall	1
Top	Wall	15
Bottom	Wall	15
Trailing-Edge	Wall	1
Tip	Wall	1
Inlet	Velocity Inlet	75
Outlet	Pressure Outlet	75
Farfield Walls	No Slip Wall	75

Table 3 Remeshing settings for the NACA0012 rotor.

Parameter	Value
Wing span	3.2m
Empty weight	15.0kg
Payload	7.0kg
Max. altitude	20000ft
Cruise speed	25m/s
Flight time	1.5-12h

Table 4 Parameters of the PX-31 Falk [27].

in the CFD simulation is shown as a dashed line. To analyse the shape of the propeller, the chord and twist angle of the propeller has been calculated in 13 positions along the shape of the propeller. The twist and chord distribution can be seen in Figure 11.

6. Simulation Setup

The propeller was put into a cylindrical test chamber to calculate the performance and the ice accretion of the propeller. For both calculations only half of the propeller was simulated to reduce the amount of calculated cells. For the propeller, two different grids were produced. The first grid is the performance calculation grid. This grid was produced in Pointwise. This grid is based on the grid setup developed in Chapter II.D.1. The surface of the propeller is represented by a structured triangular grid. The structured grid ends at 98% of the radius of the propeller, and the last two percent are represented using a unstructured mesh. The radius of the computational domain is 3 times the radius of the propeller. This was done to reduce the required computational power for the remeshing of the grid after each timer iteration step.

For the icing simulation, the computational domain excludes a cylinder at the center of the propeller. This was done to reduce computational stability of the solver when ice is present on the periodic interface. As the ice accretion on the hub of the propeller changes the shape of the propeller that has to be remeshed. During the wrapping operation in ANSYS FLUENT in the re-meshing step, the cell quality of the interfaces might be degraded when ice is present on the interface. This might prevent the proper operation of the periodic interface. For this reason a cylinder with a radius of 10% of the radius of the propeller was set at the center of the simulation domain. The hub of the propeller is attached to the cylinder, and thus does not touch the interface directly.

The distribution of the boundaries on the surface of the propeller is similar to the setup of the NACA0012 rotor. The surface of the propeller is divided into different boundaries. Because the propeller does not have a sharp edge at the tip of the propeller, the tip boundary covers the outer 2% of the radius of the propeller. The boundary at the leading-edge covers the first 20% of the chord. The length has been extended, because the stagnation point of the air on the airfoils changes with the radius of the propeller and the advance ratio of the propeller. The chord of the propeller changes,



Fig. 8 3D model of the Meijzlik 21x10 EL propeller.

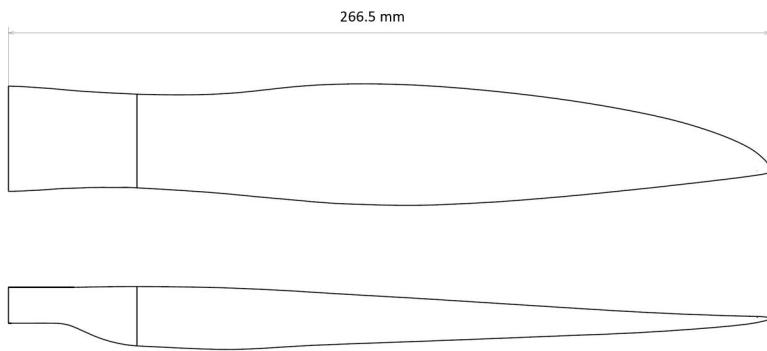


Fig. 9 Drawing of the planform of the Meijzlik 21x10 EL propeller.

as well as the airfoil of the propeller. For this reason, the cell size has to decrease towards the tip of the propeller to allow for a proper resolving of the leading-edge. In the performance calculation mesh this happens automatically, as with a structured mesh the amount of chordwise cells stays constant. Because the ice accretion mesh is at the surface a isotropic mesh with triangular cells, the refinement of the leading-edge of the outer 25 has been increased. in order to resolve this this area has been separated into its own boundaries. The boundary condition setup and the maximal cell sizes for the different boundaries can be seen in Table 5.

E. Meteorological conditions

The Federal Aviation Administration (FAA) defines two different icing envelopes for atmospheric in-cloud icing for manned aircraft in 14 CFR Part 25 appendix C [28].

The continuous maximum represents the icing conditions in a Stratiform cloud, with a extend of 17.4 nautical miles or 32.2 kilometers. This envelope is valid for flight altitudes from Sea level to 22 000 ft. The intermittent maximum represents the icing conditions in a Culmiform cloud. This cloud has an extend of 2.6nm and the envelope is valid at altitudes from 4 000 ft to 22 000 ft. In this paper, the continuous maximum was chosen, because it covers lower altitudes, where a large percentage of the UAVs are operated. The meteorological conditions chosen can be seen in Figure 12 and in Table 6. The MVD of $20 \mu\text{m}$ was chosen because Fajt et al. found in [29] the conditions at a MVD of $20 \mu\text{m}$ and a temperature of -2°C has been shown to be the worst case for a typical UAV airfoil the RG15. Therefore, three different temperatures at a MVD of $20 \mu\text{m}$ have been chosen.

III. Results

In this part, first the performance calculation and the ice accretion simulations are validated for the use for rotors on UAVs. Afterwards, the simulation methodology is applied to the calculation of a UAV propeller. The discussion of the results will be performed in Chapter IV.

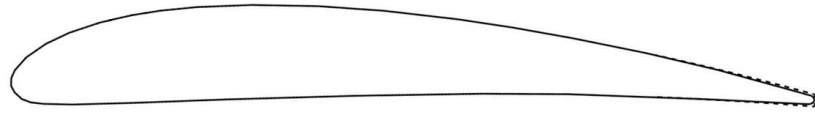


Fig. 10 Airfoil of the Meijzlik 21x10 EL propeller at 75% of the radius.

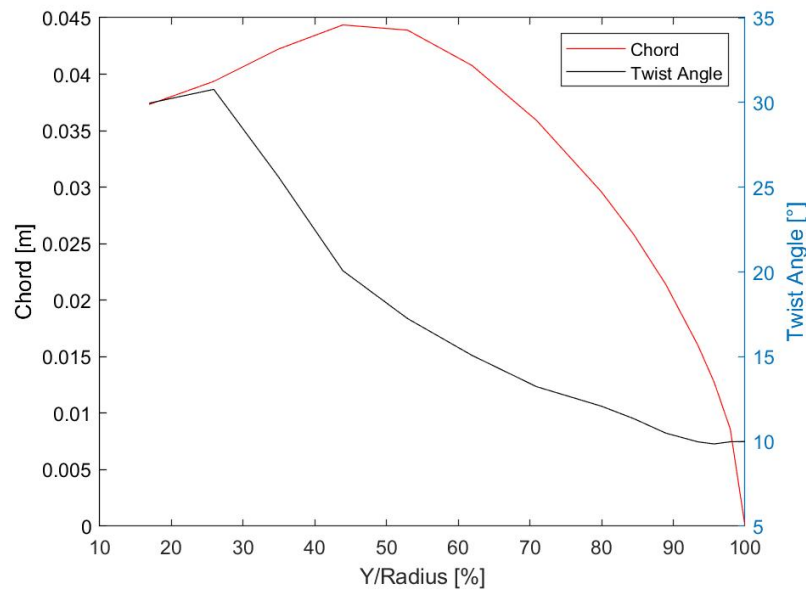


Fig. 11 Twist and chord distribution of the Meijzlik 21x10 EL propeller.

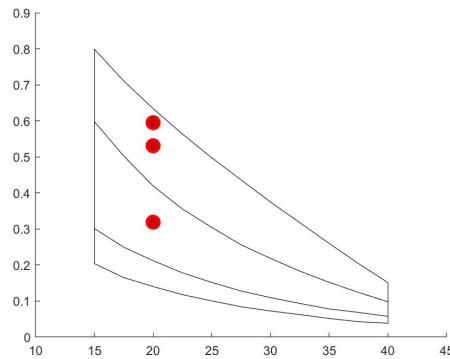


Fig. 12 The simulated meteorological points compared to the continuous in-flight icing envelope of the FAA [28].

Boundary	Boundary Condition	Max. Cell size [mm]
Leading-Edge Top	Wall	0.5
Leading-Edge Bottom	Wall	0.5
Leading-Edge Top Tip	Wall	0.2
Leading-Edge Bottom Tip	Wall	0.2
Top	Wall	5
Bottom	Wall	5
Trailing-Edge	Wall	0.2
Tip	Wall	0.2
Outside	No Slip Wall	10
Center	No Slip Wall	10
Inlet	Velocity Inlet	10
Outlet	Pressure Outlet	10

Table 5 Remeshing settings for the NACA0012 rotor.

Point	Temperature	MVD	LWC	Velocity	Duration
Point 1	-2 °C	20 μm	0.60 g/m^3	25 m/s	120 s
Point 2	-5 °C	20 μm	0.53 g/m^3	25 m/s	120 s
Point 3	-15 °C	20 μm	0.32 g/m^3	25 m/s	120 s

Table 6 Icing conditions used in the simulations for the icing of the propeller

A. Performance calculations

The first step is the calculation of the clean performance of a propeller. For this, the DA4002 propeller developed by Deters in [23] is used. This propeller was chosen because of the availability of the geometry and the experimental results data. Because this propeller has a much smaller diameter, the Reynolds number of the propeller is lower at 70.000, compared to the propeller with a Reynolds number of 200.000. This means that the viscous effects on the propeller are different. But because of the lack of experimental data for propellers in the target Reynolds number, the propeller was chosen nevertheless.

1. Grid dependency study

First a grid dependency study was performed on the DA4002 propeller. For this study, three different meshes were created, with 93, 129, and 166 cells along the chord of the propeller, as can be seen in Table 2. Those three simulations were performed using a advance ratio of 0.65. This is a typical advance ratio for the flight of UAVs. All other simulation parameters have been kept. The simulation parameters can be seen in Table 7. The laminar turbulent transition has been calculated for all simulations using X-Foil and the transition is forced for all simulations at 50% of the chord-length on the upper side. The lower side is laminar.

The results of the grid dependency study can be seen in Figures 13 and 14. As neither the thrust coefficient C_T nor the power coefficient C_P are showing a monotone trend, no Richardson-Extrapolation was performed to estimate the exact result [30]. The lack of convergence can be attributed to differences in the flowfield. For all propellers flow separation can be seen on the upper surface of the propeller, which reacts non-linear to the changes of the mesh resolution. For the thrust coefficient, all grids lie within 0.6% of each other, with grid A showing the largest deviation. For the power coefficient, all meshes lie within 0.2% of each other, with the grid B having the largest difference from each other.

Because the differences between all meshes are small, all meshes are seen as suitable in terms of accuracy. To decide for a mesh configuration, the simulation time was analysed. An overview over the simulation times is given in Table 8. Because this time is related to the number of cells in each simulation, the Grid A has the shortest simulation

Parameter	Value
Reynolds Number Re	50,000
Rotation speed n	5000 rpm
Free stream velocity u_∞	12.35 m/s
Pressure p	101325 Pa
Temperature T	288.15 K
Advance Ratio J	0.65

Table 7 Simulation parameters for the grid dependency study.

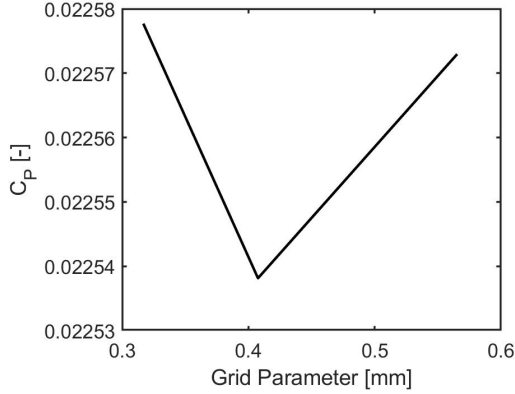


Fig. 13 Power coefficient of the grid dependency study on the DA4002 propeller.

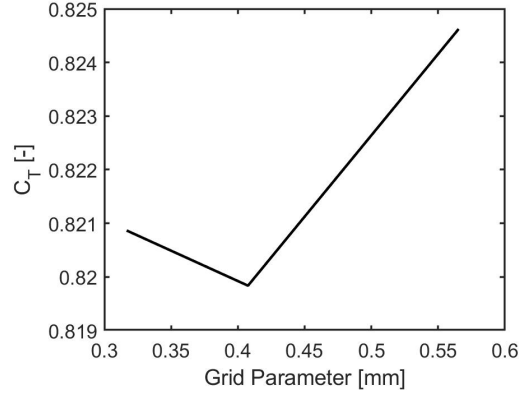


Fig. 14 Thrust coefficient of the grid dependency study on the DA4002 propeller.

time. For this reason, the Grid A is used in the continuation of this study.

Grid	Time [h:m]
Grid A	3:24
Grid B	4:45
Grid C	5:16

Table 8 Simulation times for the grid dependency study.

2. Performance analysis

In the next step, the performance of the calculation using the grid A was compared to the existing performance data gathered by Deters in [23]. An overview over the simulation parameters is given in Table 9. The simulated thrust of the grid A is 11.3% lower than the thrust of the experiment at a advance ratio of 0.65. One reason for the difference in the performance calculation could be the transition of the boundary layer from laminar to turbulent. For the simulation, the transition point has been calculated for the expected flow at 75% of the radius using XFOIL with the e^n method using a critical n of 9. This transition point has been applied to the whole length of the propeller. In a real environment, the transition point changes over the radius of the propeller, and is dependent on the turbulence level. To evaluate the calculation of the performance of the propeller over a larger range, the performance has been calculated at three different advance ratios. In Figures 15 and 16, the thrust and the power coefficient of the simulated propeller is compared to the experimental data gathered by Deters [23].

The simulated thrust is constantly underestimating the thrust, compared to the experimental data. The power

Parameter	Value
Reynolds Number Re	50,000
Rotation speed n	5000 rpm
Free stream velocity u_∞	5.7 - 13.3 m/s
Pressure p	101325 Pa
Temperature T	288.15 K
Advance Ratio J	0.3-0.7

Table 9 Simulation parameters for the grid dependency study.

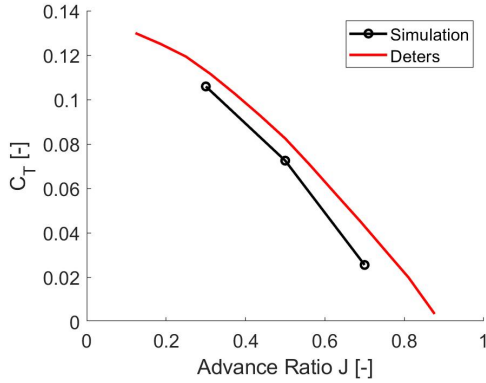


Fig. 15 Thrust polar of the DA4002 propeller compared to the experimental results by Deters [23].

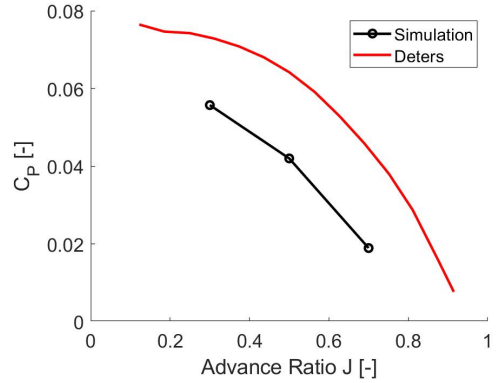


Fig. 16 Power polar of the DA4002 propeller compared to the experimental results by Deters [23].

coefficient is also always underestimated. Both changes could be related to the reduced geometry of the hub of the propeller. In the real geometry, at the center of the propeller is a motor, the shaft of the propeller and the hub of the propeller. In the simulation, the hub is simulated using a cylindrical shape and the motor is not simulated at the simulation. Another reason for the reduced thrust could be differences in the pitch angle between the experimental and the numerical propeller.

B. Ice accretion

For the validation of the ice accretion, the ice shape was calculated and compared to experimental results at two different icing conditions.

Because of the simulation of only one blade of the rotor, the effects of the wake of the rotor on the icing of the second propeller cannot be simulated. This simplification was necessary as the simulation of the full fluid domain would not be possible due to the memory constraints on the used computer. The settings for the simulation can be seen in Table 10.

Two cases are simulated, to test the simulation settings for two icing conditions. They represent typical glaze and rime ice shapes. For these reason the Runs 3 and 4 were chosen to represent the glaze ice shapes. Two experimental runs were performed, to test the repeatability of the experiments. The run 14 was chosen to represent a rime icing condition. The settings for the two simulations can be found in Table 11.

To compare the ice accretion of the experiment, the ice shapes at 95% of the radius have been compared.

The ice shape of the first case is represented well. For the case 1, the ice shape is a streamwise ice shape as it can be seen in Figure 17. The ice shape is indicative of rime ice, that freezes immediately onto hitting the surface of the airfoil. For this ice shape, the ice shape could be reproduced quite closely with the simulation. The general shape of the ice fits closely to the ice shape acquired in the experiments. The total extend of the ice seems to be close the experiment, which has a marginally larger icing extend at the leading edge of the airfoil. Therefore the simulation seems to be able to predict rime ice shapes. In case 2, the ice represents a mixed ice shape, where the central part is a glaze ice,

FENSAP	
Turbulence model	Spalart Allmaras
Boundary layer	Fully turbulent
CFL number	200
Max. number of timesteps	300
Artificial viscosity	Second order streamline upwind + cross-wind dissipation $1 \cdot 10^{-7}$
DROP3D	
Physical model	Droplets
Particle Type	Droplets
Droplet drag model	Water - default
Body forces	Rotation
Droplet distribution	Monodisperse
CFL number	20
Max. number of timesteps	120
ICE3D	
Ice - Water model	Glaze Advanced
Roughness Output	Sand-grain from beading
Body forces	Rotation
Time step	Automatic
Multi-shots	10

Table 10 Common parameters for the ice accretion study.

Simulation	Comparison Run	Temperature	Rotational Speed	MVD	Time
Run 1	AERTS 14	-15.4°C	412 rpm	28 μm	4.1 min
Run 2	AERTS 3/4	-8.3°C	492 rpm	26 μm	4 min

Table 11 Settings for the ice accretion runs

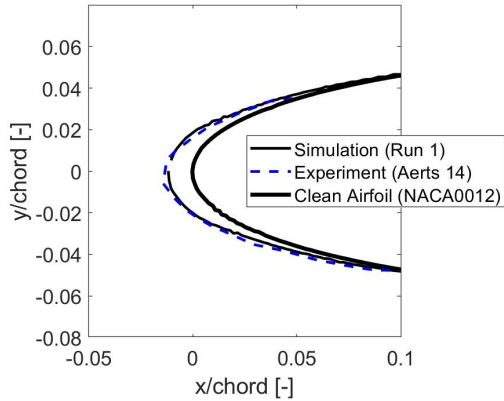


Fig. 17 Ice shape of ice accretion validation case 1.

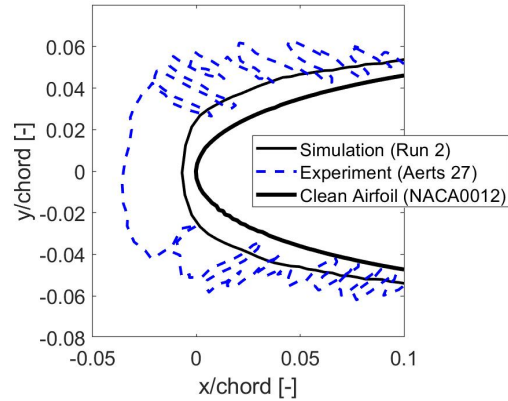


Fig. 18 Ice shape of ice accretion validation case 2.

with feathers outside. ANSYS FENSAP-ICE seems not to capture the ice shape. The most likely reason for this is an insufficient mesh size. The mesh size could be too large, to resolve all the feathers in the ice shape in this case. The large difference in the area of the predicted ice shape to the measured ice shape could also have other reasons. To validate the proper settings of the multi-shot simulation, the calculation was done in one step, to verify whether the interactions between the ice shape and the airflow had any influence on the ice accretion. The results of the calculation in one step can be seen in Figure 19. The results show, that the total ice mass stays similar, but the difference in the extend of the ice shape can be seen. The simulation with multiple iterations creates an ice shape that has a small size at the front of the airfoil, and more ice has accumulated on the top and bottom of the airfoil, leading to a thicker ice shape after 1% of the chord-length of the clean airfoil. The change in the airflow around the rotor will influence the ice accretion process. Because this is not regarded in the single step simulation, the ice shape in the single step simulation is more streamlined.

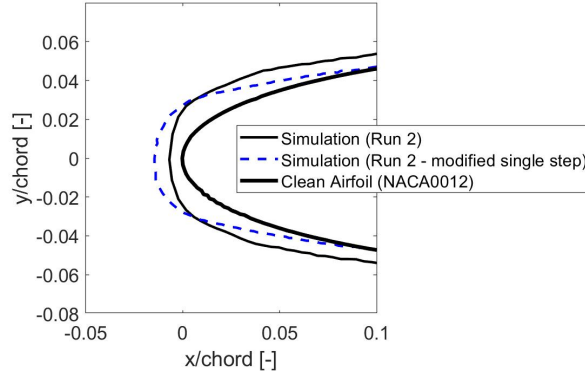


Fig. 19 Ice shape of ice accretion in the validation run 2 compared to a simulation with one icing step.

The reasons for the large difference in the ice shape between the simulation and the experiment could be the difference in the geometry. In the simulation only the blade from 50% of the radius outward is represented. Because of the centrifugal forces of the rotation, water in the center will flow outward before freezing. Therefore, the thickness of the ice in the outer parts of the rotor will increase. Another reason could be the feather shape of the ice outside the center. This cannot be represented in the simulation, because the chosen mesh resolution and the amount of icing steps is insufficient. The mesh on the surface of the NACA0012 rotor after 10 icing steps can be seen in Figure 20. Glaze ice is always more complicated to simulate correctly, as the heat transfer needs to be calculated in higher detail, compared to a rime ice shape [31] and [32]. In a future work the proper resolution could be achieved by only simulating the flow on a small slice of the rotor, and disregarding the rotation, in order to find the proper resolution for the ice shape. Because this mesh setup would be very dissimilar to the mesh of the propeller which is the main part of this study, this was not done as a part of this study.

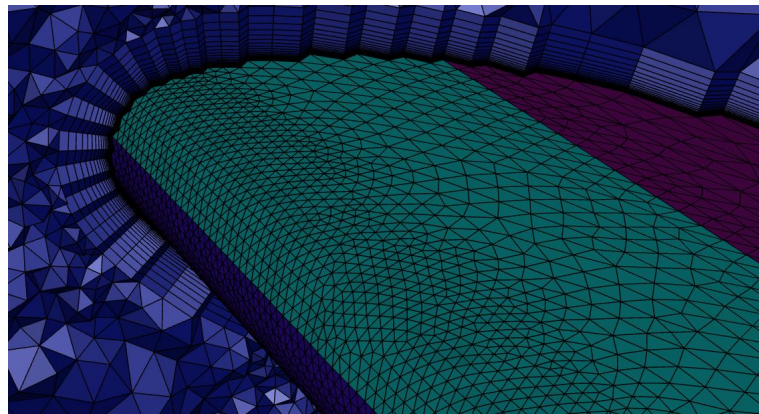


Fig. 20 Mesh of the iced NACA0012 Airfoil in simulation run 2.

C. Propeller

1. Ice accretion

The settings for the ice accretion studies can be seen in Tables 12 and 13 and 14. The results show that the temperature has a large influence on the ice shape of the propeller.

FENSAP	
Turbulence model	Spalart Allmaras
Boundary layer	Fully turbulent
CFL number	350
Max. number of timesteps	500
Artificial viscosity	Second order streamline upwind + cross-wind dissipation $1 \cdot 10^{-7}$
DROP3D	
Physical model	Droplets
Particle Type	Droplets
Droplet drag model	Water - default
Body forces	Rotation
Droplet distribution	Monodisperse
Boundary layer	Fully turbulent
CFL number	20
Max. number of timesteps	120
ICE3D	
Ice - Water model	Glaze Advanced
Roughness Output	Sand-grain from beading
Body forces	Rotation
Time step	Automatic
Multi-shots	10

Table 12 Setup parameter study for the simulation of the iced propeller performance.

Parameter	Value
Reynolds number Re	50,000
Rotation speed n	5000 rpm
Free stream velocity u_∞	25 m/s
Static pressure p	95 500 Pa
Temperature T	0°C
Advance Ratio J	0.65

Table 13 Setup parameter study for the simulation of the iced propeller performance.

2. Temperature -2°C

The ice shape at a temperature can be seen in Figure 21. Ice accretion has only happened in the central part of the propeller. The tip of the propeller is almost ice-free. This is due to the increase of the stagnation temperature by the

Run	Temperature	Rotational Speed	MVD	Time
Run 1	-2°C	5000 rpm	20 μm	120 s
Run 2	-5°C	5000 rpm	20 μm	120 s
Run 3	-15°C	5000 rpm	20 μm	120 s

Table 14 Settings for the ice accretion runs.

rotation of the propeller. At the simulated rotational speed of the propeller, the speed of the tip of the propeller is 139.6 m/s. This equates to a Mach number of 0.41. At this speed, the temperature of the air at the stagnation point rises to temperatures above 0°C. This can be seen in Figure 22. Therefore no ice accretion at the leading-edge of the airfoil is observed close to the tip of the propeller. Behind the leading-edge, the friction between the propeller and the air is heating up the air and is preventing the ice accretion. Closer the center of the propeller, friction heating is low, and therefore ice can accrete at the center of the propeller. The ice forms a span-wise horn, starting at 92% of the radius which is growing inwards. At less than 48% of the radius of the propeller, ice starts to accrete at the top of the propeller. The ice shape is typical for a glaze ice shape. In Figure 21 the ice shapes can be seen in comparison to the clean airfoil. The contour of the geometry is given for the ice shape at 50%, 80% and 90% of the radius of the propeller. On the bottom left image, the detail of the ice shape at the leading-edge of the propeller is given. The ice shape is colored in white, while the propeller is grey in the image.

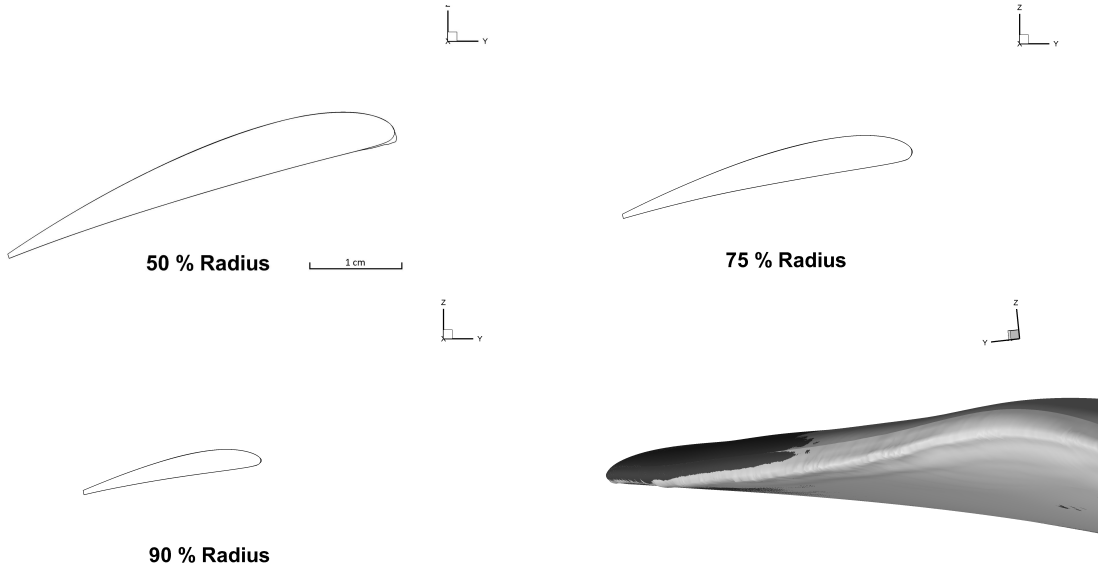


Fig. 21 Ice shapes of the ice accretion Case 1 at -2°C on the propeller.

3. Temperature -5 °C

The ice shape at a temperature of -5°C can be seen in Figure 23. At this temperature, the ice accretion happens along the whole propeller. For the same reasons as with the -2°C case, the stagnation point of the propeller is mainly ice free from 75% of the radius outward. The ice once again shapes two span-wise horns. The horn at the top of the propeller starts at 87% of the radius and the horn at the bottom starts at 98% of the radius of the propeller. This is a typical ice shape for glaze ice. The ice shapes can be seen in Figure 23.

In Figure 24, the icing contour at 74% and 75% of the radius are compared. Here the difference small differences in the choice of the cut plane for the contours makes can be seen clearly. The Cut at 74% of the radius shows two horns, while the height of the spanwise horn at the top of the propeller is smaller at 76% of the radius.

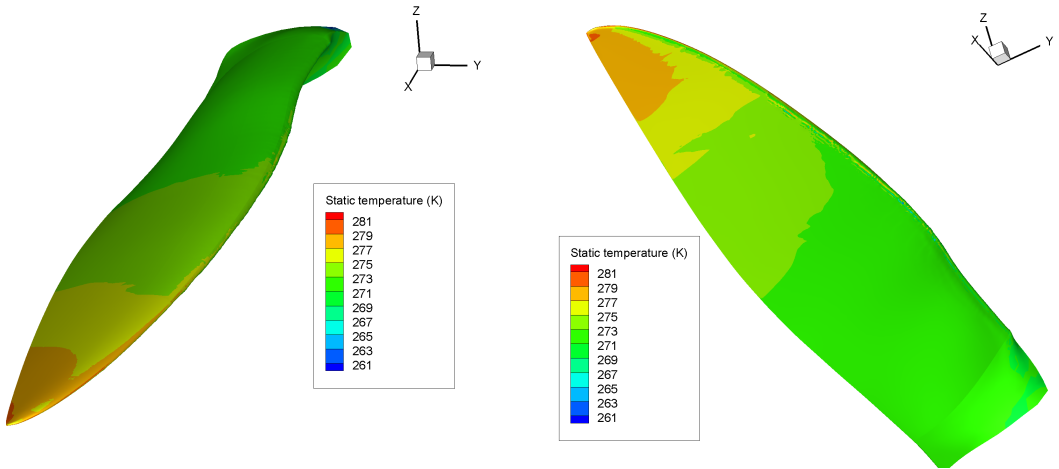


Fig. 22 Surface temperatures of the propeller in simulation Run 1 at -2°C .

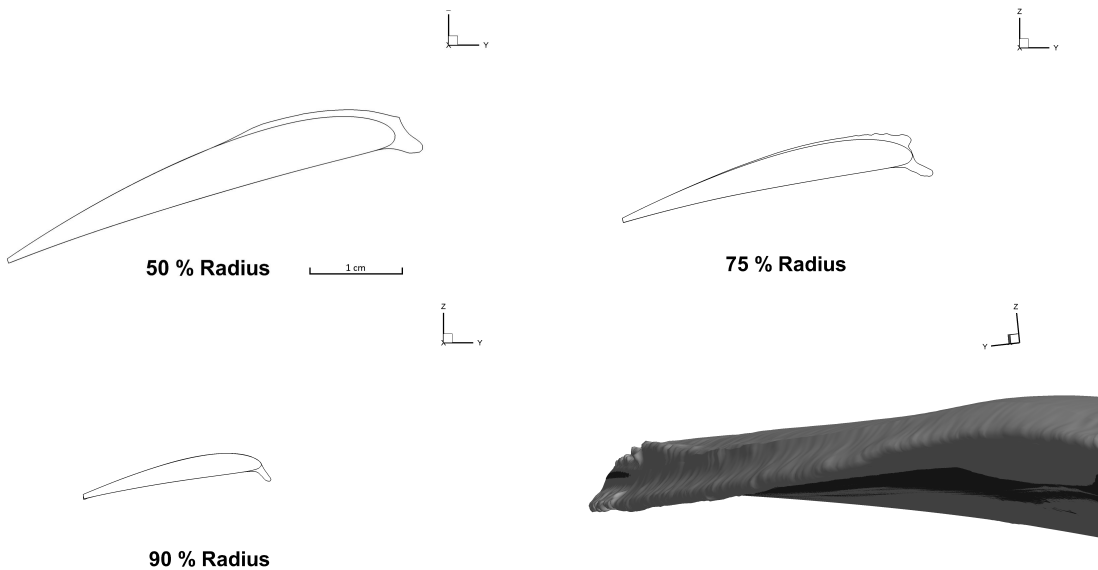


Fig. 23 Ice shapes of the ice accretion simulation run 2 at -5°C on the propeller.



Fig. 24 Ice shape at 74 % and 76% of the radius on the propeller in simulation run 2.

4. Temperature -15 °C

At a temperature of -15°C, the ice shape is very uniform, without the creation of horns. The ice shape can be seen in Figure 25. The full leading-edge of the propeller is covered in ice. This ice shape does represent a typical rime ice shape. The ice shape shows little change along the span of the propeller. The ice growth shows a great resemblance to the collection efficiency of the propeller. This happens, because most of the droplets freeze close to the point of impact with the propeller. The collection efficiency of the stagnation point is growing with the radius of the propeller and reaches a maximum at a radius of 91 %. The collection efficiency on the surface of the propeller can be seen in Figure 26. The collection efficiency decreases, because the increased sweep angle of the propeller is decreasing the velocity of the air in the normal direction of the leading-edge of the propeller. The ice mass at -15°C is lower than the ice mass at -5 °C, because the LWC at -15 °C is lower, compared to the LWC at -5 °C. While at -15 °C, all water that hits the surface will freeze, a percentage of the impinging water at -5 °C 43% of the water will shed from the propeller, without freezing to the surface.

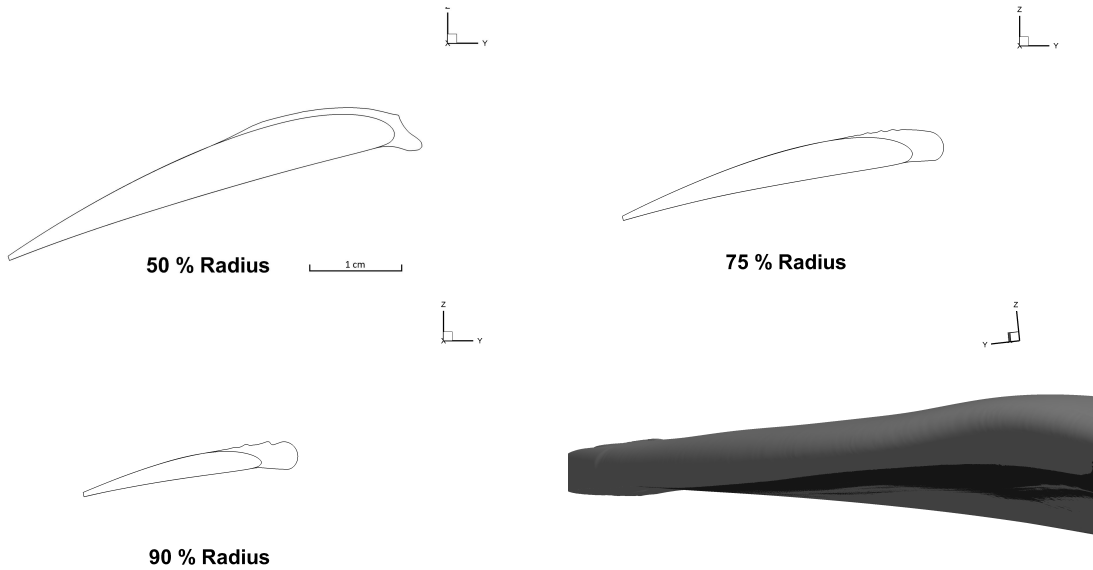


Fig. 25 Ice shapes of the ice accretion simulation run 3 at -15°C on the propeller.

Temperature	Ice mass [g]
-2 °C	16.5
-5°C	63.2
-15°C	62.8

Table 15 Ice mass of the different ice accretion simulations.

5. Performance degradation

The performance of the propeller after the ice accretion was analyzed. For the final simulation, the aerodynamic properties of the iced propeller shapes were analysed. The final shape of the ice was taken, and remeshed in ANSYS Fluent. The aerodynamic performance of the propeller was analysed and compared to the simulation of the clean propeller. For the better comparison between the different icing conditions, all simulations have been conducted under the same conditions. This includes the temperature, which is set to 0°C. This means, that the different Reynolds numbers at the different temperatures at which the ice shapes have been formed are not regarded in the calculation of the aerodynamic properties. The simulation settings for this run can be seen in Tables 16 and 17.

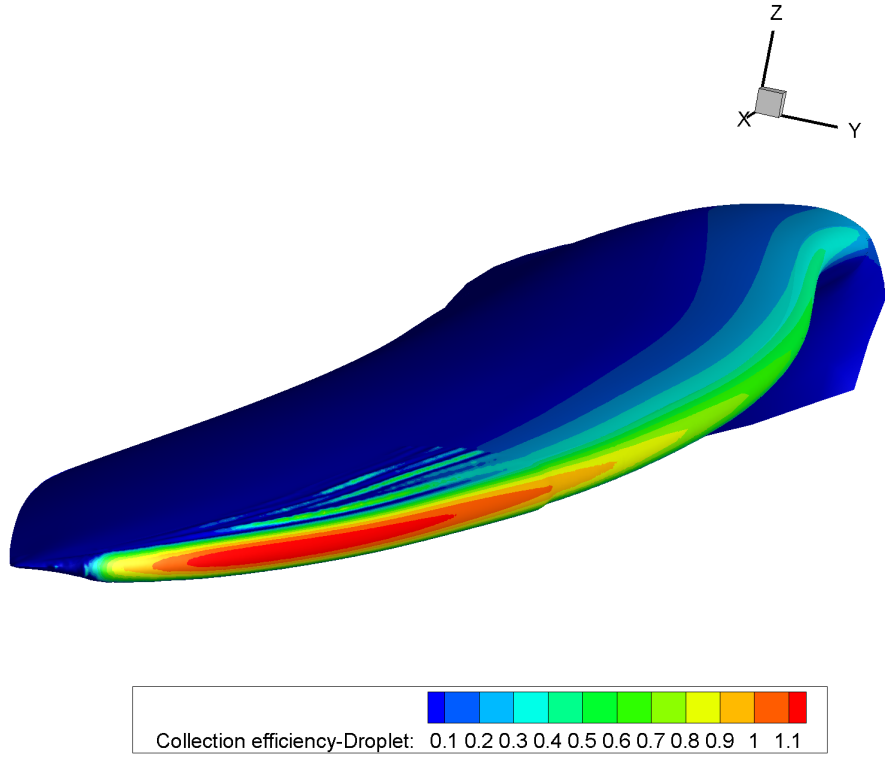


Fig. 26 Collection efficiency on the surface of the propeller in simulation run 3 at -15 °C

FENSAP	
Turbulence model	Spalart Allmaras
Boundary layer	Fully Turbulent
CFL number	350
Max. number of timesteps	5000
Artificial viscosity	Second order streamline upwind + cross-wind dissipation $1 \cdot 10^{-7}$

Table 16 Setup parameter study for the simulation of the iced propeller performance.

Parameter	Value
Reynolds Number Re	50,000
Rotation speed n	5000 rpm
Free stream velocity u_∞	25 m/s
Static pressure p	95 500 Pa
Temperature T	0°C
Advance Ratio J	0.65

Table 17 Simulation point for the performance calculation runs.

6. Clean propeller

First, the performance of the clean propeller was calculated. The values of the shear stress on the propeller can be seen in Figure 27. At the flight velocity of 25 m/s and a rotation rate of 5000 rpm, the propeller produces 20.2 N of thrust, and requires 560 W of power from the motor.

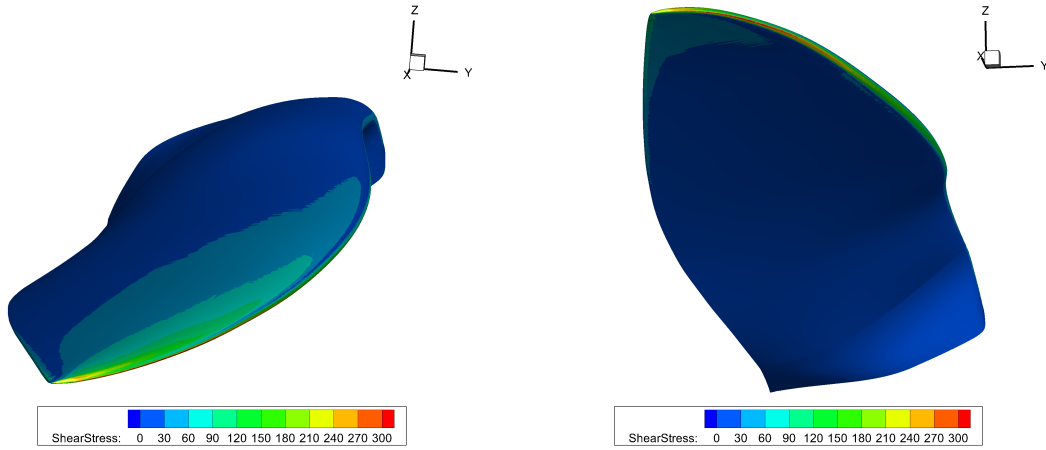


Fig. 27 Shear stress on the clean propeller.

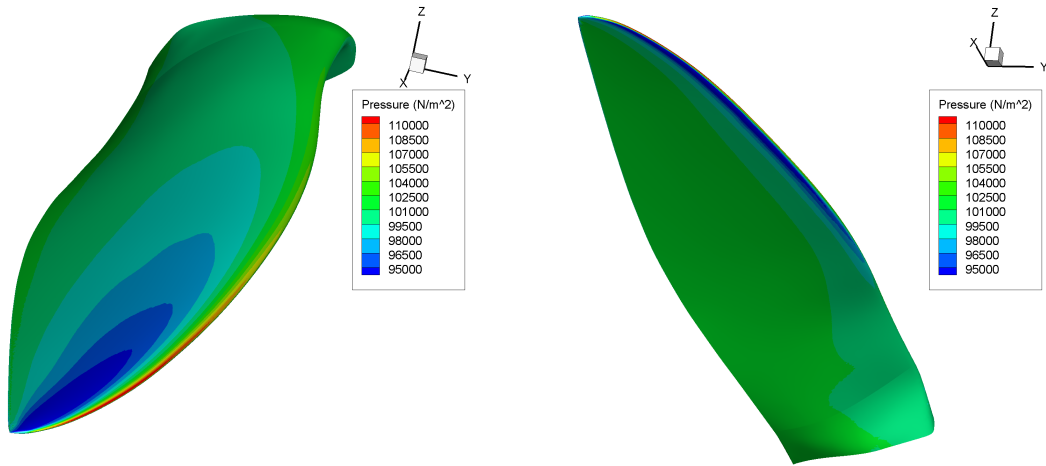


Fig. 28 Pressure on the clean propeller.

7. Temperature -2°C

At a temperature of -2°C, the least amount of ice has accumulated on the airfoil. This corresponds with the least amount of performance degradation compared to the clean configuration. This leads to a thrust reduction of 4.1% compared to the clean configuration. The power the engine has to provide to turn the propeller has increased by 9.1 %. The decrease in the thrust of the propeller is due to the reduced lift of the propeller. The lift is decreased by the accumulated ice, because the ice shapes disturb the airflow around the airfoil. This happens especially at the leading-edge of the airfoil. The flow around the airfoil can be seen in Figure 29. The ice shape created by the ice cause a large disturbance in the airflow and causes a large separation between the airflow and the propeller. While the separation at the center also occurs for the clean propeller, the large wake area in the middle of the propeller is created by the ice shape. The red surface is an iso-surface with a constant turbulent viscosity of 0.001 N s/m^2 .

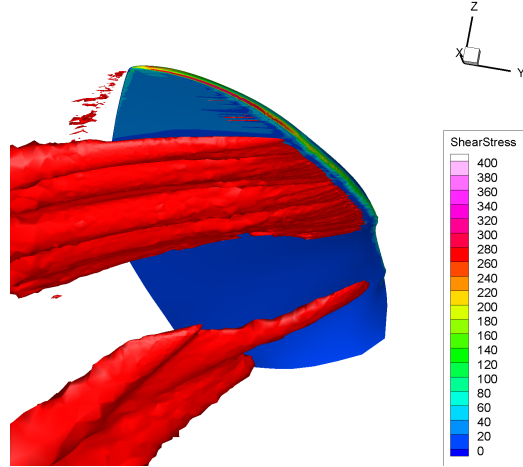


Fig. 29 Visualization of the wake of the propeller at -2 °C.

8. Temperature -5 °C

At this temperature, largest reduction in the performance of the propeller is observed. The thrust of the propeller is reduced by 47% and the power coefficient of the propeller is increased by 44%. This leads to a reduction in the efficiency of 63%. This large decrease in the efficiency of the propellers is presumably caused by the large horns created in the ice shape. They disrupt the flow of the air and they decrease the thrust of the propeller. Because the angle of attack of the airflow at the propeller is dependent on the thrust of the propeller, because of the induced velocity of the propeller, a reduce in the thrust leads to a increase in the angle of attack of the propeller. Combined with the reduced stall angle of a iced propeller, this makes the propeller stall, which drastically reduces the thrust of the propeller. In Figure 30, the shear stress on the leading-edge of the propeller is shown, for the iced case, and the clean comparison case. It can be seen, that the ice is increasing the friction forces on the ice horns, and is thus decreasing the performance of the propeller.

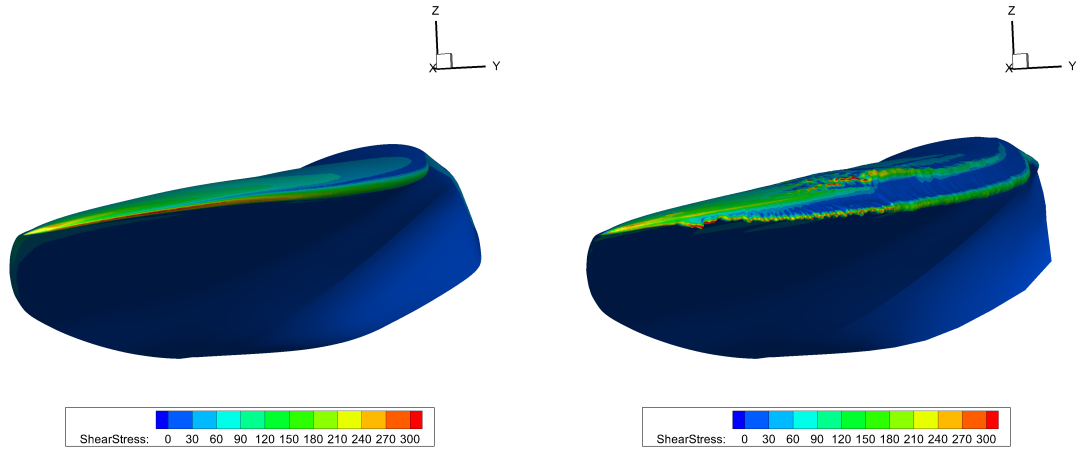


Fig. 30 Shear stress comparison between the clean propeller on the right and the propeller of icing Case 3.

9. Temperature -15 °C

At a temperature of -15°C, the ice has accumulated on the full length of the leading-edge of the propeller. The efficiency lost at this temperature is driven by the increase of the power coefficient by 29.5%, while the thrust has been reduced by 9.5%. The reason for this behavior is assumed to be the increase in the drag of the airfoil. The ice shape is streamlined, with very limited disturbances to disrupt the airflow over the propeller. For this reason, the thrust of the propeller is still similar to the clean propeller. The ice shape does however increase the area of the propeller

substantially, and the airflow over the larger area does increase the drag of the propeller. Furthermore, the ice increases the thickness of the propeller, and increases the radius of the leading-edge of the propeller. Those two aspects contribute to an increase in the drag of the propeller. The larger area of the iced propeller shape does also have a positive influence on the thrust of the propeller.

10. Overview

The different temperatures had very different influences on the aerodynamic performance penalties of the propeller. The Table 18 given an overview over the different changes in the aerodynamic performances of the propeller. The Figure 31 gives the plot of the changes of this values over the temperature. It is clear, that not only the total ice mass is relevant for the loss of efficiency, but also the shape of the ice.

Case	C_T change [%]	C_P change [%]	η change [%]
-2°C	-4.1	9.9	12.7
-5°C	-46.4	44.3	62.9
-15°C	-9.5	29.5	30.3

Table 18 Performance change compared to the baseline.

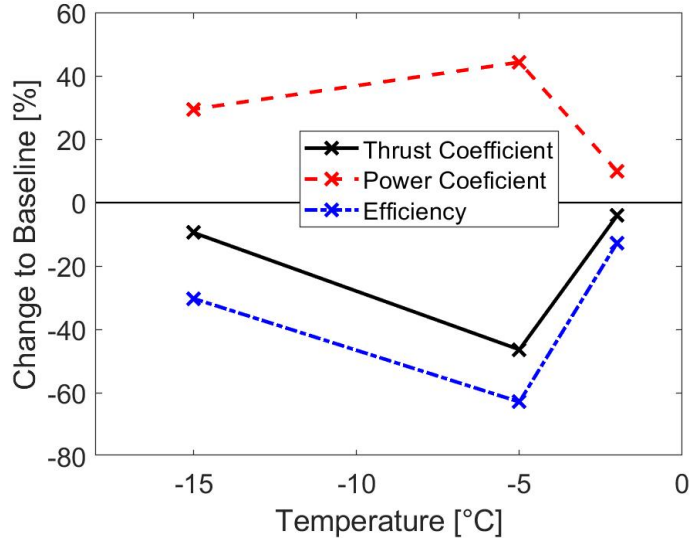


Fig. 31 Change of the aerodynamic performance of the propeller with for different temperatures.

D. Ice protection system loads

For the design of an ice protection system, the information about the required power is necessary. For this simulation, the conditions of the run with the lowest temperature was taken. The lower the ambient temperature, the higher the loads on the icing protection system, as it must heat the fluid-film to 0°C. For this reason, the case with the lowest temperature is the worst case scenario for the IPS. Two different conditions for the IPS System have been calculated. In the running wet condition, the temperature of the surface of the propeller is set to be 0 °C. The fluid hitting the surface may evaporate, or it may flow to the backside of the propeller, where it will shed back into the air. In the fully evaporative condition, the fluid needs to be evaporated within the impingement zone. This leads to a higher required heat flux by the IPS. Because the water will be evaporated within the impingement zone, the heated area is smaller. The power required by the IPS can be seen in Table 19. The required heat flux in fully evaporative conditions is 48% higher, while the maximum heat flux is 374% higher, compared to the running wet condition. The maximum heat flux is a

key design criteria as it influences how much the layout of the heating zones. The distribution of the required heat flux can be seen in Figure 32. It is clear, that the IPS needs to be focused on the leading-edge of the propeller as here the maximum heat flux requirement is present. In the fully evaporative mode, only regions where water impinges the propeller need to be heated, while under running wet conditions the whole propeller needs to be heated, because the fluid will flow towards the back of the propeller. Without heating pads towards the back, the water will freeze there. The maximum load happens towards the tip of the propeller, as here the air velocities will be the highest. Because the extend of the maximum value for the heat flux is spatially limited, in real world situations, the maximum load provided by the IPS may be lower, as thermal conductivity of the surface will spread the heat flow. Furthermore, the leading-edge may be operated under running wet conditions, and the water will be evaporated further down the propeller.

Situation	Required power [W]	Maximum heat flux [kW/m^2]
Running wet	167.5	46.7
Fully evaporative	248.6	174.4

Table 19 Results of the IPS load estimation from simulations at -15°C and a MVD of 20 μm .

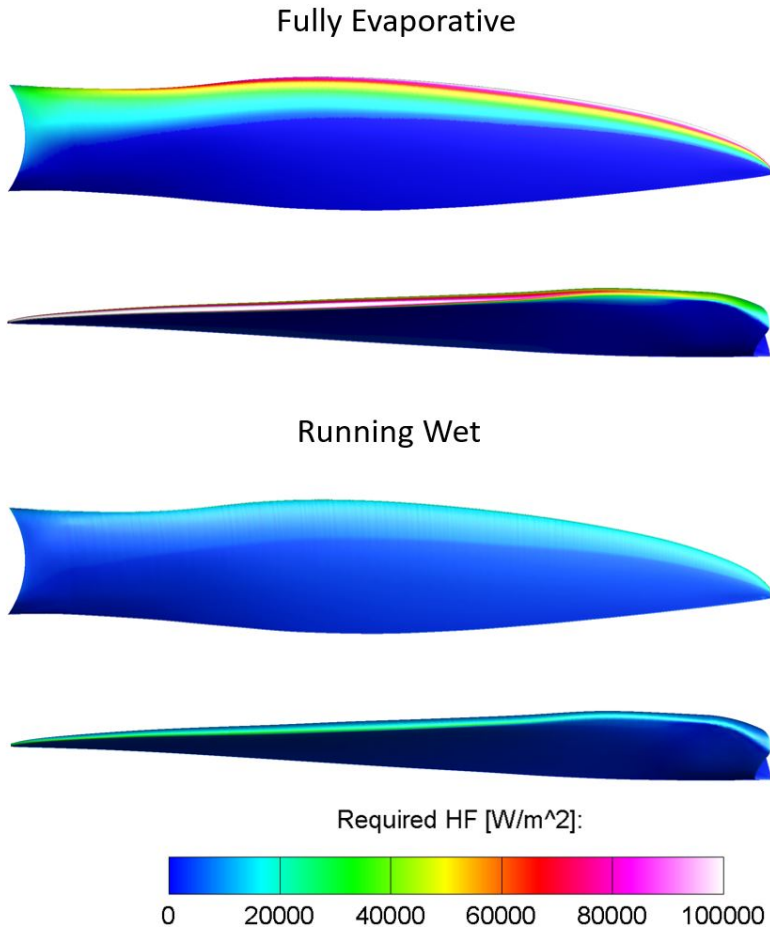


Fig. 32 Results of the IPS calculations for the case 3 at -15 °C.

IV. Discussion

In this section, the results of the previous sections are discussed and possible explanations for the phenomena are presented.

A. Ice accretion

The ice accretion on the propeller has been analysed in three different meteorological conditions, which produced three different ice shapes. At temperatures closer to the freezing point only minimal ice accretion and the creation of ice roughness has been observed. At lower temperatures, first a glaze ice shape with spanwise horns has been observed, and than at -15°C , the ice shape represented a stream-wise ice shape. For a typical UAV airfoil, RG-15, simulations have shown that at -2°C the performance is impacted the most by the ice accretion, while at -5°C , the ice shape starts showing a stream-wise ice shape [29]. The reason for the difference in the ice accretion between two different parts of the same aircraft is the increased friction of the propeller. The increased velocity of the airflow over the propeller compared to the wing increases the Mach number. The Mach number for the tip of this propeller is 0.4, while the Mach number of the wing is only 0.1. This increased Mach number leads to compressibility effects playing a greater role for the airflow. For example the stagnation temperature increases with the increased Mach number of the propeller. For this reason, the temperature of the leading-edge of the propeller at -2°C is greater than 0°C and thus no ice can form on the leading-edge of the propeller. Another reason is the friction heating of the air as it flows over the surface of the propeller. Therefore, the rotation speed of the propeller needs to be treated as a separate parameter in the ice accretion of a propeller. If the rotational speed of the propeller is reduced, the reduced Mach number would lead to a reduced stagnation temperature, and thus allow for the ice accretion even at higher temperatures. Another effect of the change in the rotational speed is the change in the Reynolds number. Decreased Reynolds numbers could lead to an increase in the heat transfer between the fluid film and the air, and thus increasing the glaze icing, compared to higher Reynolds numbers.

One effect that has been disregarded in the current analysis of the ice accretion is the ice shedding. This describes the process, where a part of the ice breaks off the main ice shape. This is a common phenomenon during the icing of propellers, as the high centrifugal forces and the vibrations caused by nonuniform ice accretion will increase the likelihood of ice shedding. For the analysis of the ice shedding, the adhesion forces of the ice on the surface and the cohesion forces inside the ice have to be calculated. Ice shedding can be dangerous, because the ice that is detaching from the propeller can hit the UAV, and cause damage to it. If the ice shedding does not happen symmetrically on all propeller blades, vibrations can be caused. These vibrations can be caused by the mass imbalance between the propeller blades, or by the difference in the aerodynamic properties between the propeller blades, and the subsequent differences in the aerodynamic forces.

B. Performance simulation

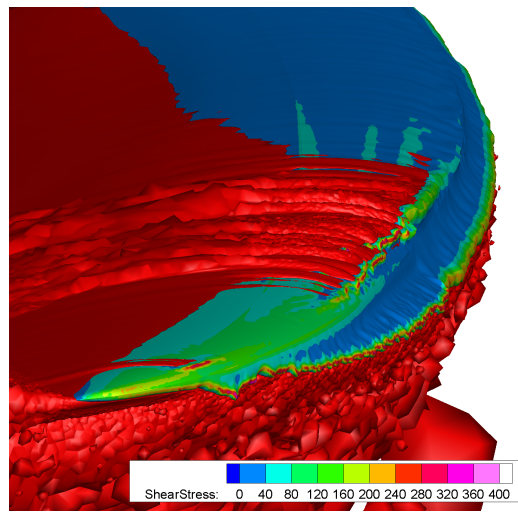


Fig. 33 Detail image of the tip of the propeller at a temperature of -5°C .

Ice accretions have a large influence on the performance of the propeller. While the ice accretion and thus the performance degradation at a temperature of -2°C is comparatively low, the ice accretion at a temperature of -5°C is the largest, that has been found in the simulations. The most likely reason for this are the developed spanwise horns on the propeller. The influence of these horns is shown in Figure 33. Here an iso-surface of the turbulent viscosity is shown. This can be used, to differentiate between regions of low and high turbulence in the airflow. This can lead to an earlier detachment of the flow from the propeller, and thus reduce the aerodynamic performance of the propeller. It can be seen, that the spanwise horns on the bottom of the propeller lead to a detachment of the airflow over the propeller along the full length of the propeller. On the top, the horn shape is smaller, and thus the areas with high turbulent viscosity are smaller. If the shear-stress on the surface of the propeller is analysed, it can be seen, that the shear-stress on the surface of the propeller is significantly increased in the areas where ice is present. This increase in shear-stress will increase the drag of the airfoil, and thus decrease the thrust of the propeller as well as it will increase the required power to operate the propeller. The stream-wise ice shape that is present at -15°C has a smaller influence on the performance of the propeller. Here the main influence on the performance of the propeller is the increased drag of the airfoil, which leads to a reduced performance of the propeller. Because the mesh convergence study performed on the DA4002 propeller was not fully conclusive, and does not cover the iced propellers, a more detailed mesh convergence study needs to be performed in the future.

The ice accretion on the surface of the propeller has been analysed for a time frame of 120s. In reality, a UAV like the PX-31 Falk will need over 21 minutes to traverse even a stratiform cloud. These clouds are used as a reference of the continuous atmospheric icing envelope by the FAA [28]. So the maximum icing extend could be much larger, if the flight of the UAV through the icing conditions continues.

In a cumuliform cloud used for the intermittent icing envelope, the LWC of the cloud is much larger, and therefore, the ice accretion could probably create a similar ice cover in significantly less than 120 s. A higher LWC is usually associated with ice shapes, that are more likely to be glaze ice shapes. Therefore, in most cases they will lead to an increase of the aerodynamic performance penalties. In this study, a ice accretion time of 2 minutes was chosen, because the ice shapes already have a significant size, and the aerodynamic penalties are large. For many multi-rotor UAVs, a efficiency loss of 63% at the propeller might be enough, to reduce its flight capabilities beyond the minimum required for a stationary flight. Most fixed wing UAVs will also lose the ability to climb, or to keep its altitude, especially, if the ice accretion on the rest of the UAV is taken into account.

C. Icing protection system

The calculation of the icing protection system loads presented in this work have not been validated against experiments, but the methodology used has been used to predict the required icing protection systems for the wings of UAVs by Hann et al. [31]. For this reason, they need to be validated against the required icing protection system loads of a propeller in a future work. The results show, that to prevent the ice accretion on the propeller of an UAV, a very high maximum heat flux is required at the leading-edge of the propeller, especially towards the tip of the propeller. This heat flow could be created by electro-resistive heating elements in the leading-edge of the propeller. In this simulation the required heat flux was calculated without taking heat conductivity into account. To decrease the high maximal heat fluxes at the leading-edge, the propeller could be created from a material with a high thermal conductivity. Because the aim of the IPS is to heat the propeller to an uniform temperature, the effects of heat conduction can be used to distribute the heatflux from the heating element to the surface of the propeller.

D. Comparison with literature

There is only a very limited amount of experiments, that have been conducted, with which the results of the study can be compared. The ice accretions at the experiments on the ice accretion on a UAV propeller performed by Liu et al. [17], also showed a rapid ice growth at the leading-edge of the propeller. The thrust coefficient did decrease in this case, and the power coefficient did rise rapidly. In the meteorological conditions that did not produce a glaze ice shape with spanwise horns, the reduction of the thrust coefficient was only small. This does fit to the findings of this work, as in this work also the thrust coefficient was seen to be reduced in the test case at -5 °C, while the power coefficient was rising in all cases.

E. Uncertainties

As described in the previous chapters, there is very little experimental data available for the validation of the simulation models. Therefore, the aerodynamic performance has been calculated using a test case with a much lower Reynolds number. The ice accretion on the other hand has been validated using a experiment with a much larger Reynolds number. Because the Reynolds number is different, the impact of the viscous forces can not be correctly verified. Furthermore, the mesh close to the wall of the simulations will be different. Because the height of the first prism cell is fixed by the maximum y^+ value, the height of the first cell is different. Furthermore the performance calculation of the iced calculation could not be validated. Here experiments for the performance of propellers with ice shapes need to be executed to validate the ice shapes.

In the cases analysed in this present study, all droplets in the fluid had the same diameter. In most real cases, the droplets will have a range of different sizes, which could influence the shape of the ice. To analyze the influence of this setting, either further simulations with a droplet size distribution or experiments with a dispersed droplet distribution will need to be performed.

The ice accretion was only calculated using one advance ratio. In a real environment one would expect the rotational speed of the propeller to change and therefore, the advance ratio to change. This will be due to the reduced thrust created by the propeller and therefore the controller would increase the power to the propeller to keep the speed of the aircraft steady.

Only the propeller has been evaluated. Ignoring the influence of the fuselage can make a large difference. It is common for the propeller of a UAV to be in the so called pusher configuration, where the propeller is mounted behind the fuselage. In those cases, the fuselage will have a large influence on the ice accretion of the propeller. The smooth airflow before the propeller is disturbed, as the propeller operates for a large part inside the boundary layer of the propeller. Furthermore the droplet distribution will no longer be uniform behind the fuselage. Here a steady approximation will no longer be valid, as the flow conditions will be dependent on the angle of the propeller in its rotation. These uncertainties show that to increase the confidence in the simulations, more experimental data is necessary to validate the used simulation models.

F. Relevance

The analysis of the ice accretion of the propeller in different meteorological conditions is important for the development of icing protection systems for UAVs. For the wings of UAVs, a promising concept has been developed using an electro-thermal approach. This system is able to autonomously detect and remove ice on the wing of the UAV by operating intermittently to detect the ice accretion on the UAV. This work provides the groundwork to apply this system to the propeller of the UAV.

The identification of the -5°C / MVD $20 \mu\text{m}$ worst case icing condition for the propeller is important for the development of the IPS. This allows the future simulations and experiments to focus on the right simulation conditions. As it was outlined by Hann et al. in [13], the correct simulation point is one of the challenges in the development of IPS Systems for UAVs.

V. Conclusion

A process for the calculation of the ice accretion of the propeller of a small-medium UAV was developed. CFD simulations were used to calculate the ice accretion and the performance penalties of a propeller. The propeller in this study is a Mejzlik 21X10 EL propeller, used on the Maritime Robotics PX-31 Falk, a fixed-wing UAV with a wingspan of 3.2m.

First an overview over some of the existing icing experiments performed was conducted. During this, a database of 71 icing experiments was created. In this database, the icing experiments are divided into icing experiments that capture the impingement of the water on the surface, experiments that create the shape of the ice, and experiments for the performance degradation of the iced airfoil. Most of those experiments are focused on manned aircraft, and are done at Reynolds numbers above the typical Reynolds numbers of an UAV.

A large challenge during the development of the process to calculate the ice accretion on a propeller has been the small amount of ice accretion experiments performed on propellers at a similar Reynolds number. For this reason, the next step in the development of a process to calculate the icing of a UAV is the validation of the results by performing ice accretion experiments on a propeller in an icing wind tunnel, and execute tests to estimate the performance penalties of the ice on the propeller. This data can be used to refine the mesh and simulation settings of the process. This will

lead to an increase in the credibility of the results of the ice accretion results. Especially the use of a fully turbulent boundary layer over the ice needs to be validated for the use at such low Reynolds numbers.

The simulation of the performance of the propeller of an UAV has been conducted using the tool ANSYS FensapICE. The results show that at different temperatures the ice morphology changes. This different ice shapes have different impact on the performance of the propeller. The largest reduction in the efficiency of the propeller has been found at a temperature of -5°. At higher temperatures the accumulated ice mass on the propeller is reduced because the friction heating between the propeller and the air heats up the temperature of the airflow above the freezing point at the tip of the propeller. This leads to a reduction of the total ice mass on the propeller. At lower temperatures the ice forms a streamlined ice shape which has a lower impact on the performance of the propeller.

In all cases the efficiency of the propeller is reduced by a large margin of up to 63%. This highlights the need for further research in the icing on the propeller of UAVs. Methods to mitigate this hazard need to be developed to enable UAVs to fly in adverse weather conditions. The required heating loads for an anti-icing system have been calculated. With this data, an electro-resistive anti-icing system could be developed.

And for UAVs without a icing protection system, the data can be used in the route-planing of the autopilot, to avoid areas, where the icing would be a threat to the UAV. The developed process could be applied to the calculation of the icing on the propellers of multi-rotor UAVs, for which the thrust of the propellers is directly responsible for the lift of the UAV. This makes the multi-rotor UAVs more vulnerable to icing on the propeller, as any loss in lift could lead to immediate loss of control of the UAV.

Acknowledgements

This work has received funding from the Research Council of Norway under grant numbers 223254 Centre for Autonomous Marine Operations and Systems (NTNU-AMOS). Further funding was received from the Norwegian Research Council FORNY, grant number 284649, and from the Regionalt Forskningsfond Midt-Norge, grant number 285248. The numerical simulations were performed on resources provided by the National Infrastructure for High Performance Computing and Data Storage in Norway (UNINETT Sigma2) on the Vilje supercomputer, under project code NN9613K Notur/NorStore. We would also like to thank Mejzlik for their cooperation.

References

- [1] Leary, W. M., *We freeze to please: a history of NASA's icing research tunnel and the quest for flight safety*, National Aeronautics and Space Administration, 2002.
- [2] Hann, R., and Johansen, T., “Unsettled Topics in Unmanned Aerial Vehicle Icing,” *SAE International, SAE EDGE Research Report EPR2020008*, 2020. <https://doi.org/10.4271/epr2020008>.
- [3] Gent, R. W., Dart, N. P., and Cansdale, J. T., “Aircraft Icing,” *Philosophical Transactions: Mathematical, Physical and Engineering Sciences*, Vol. 358, No. 1776, 2000, pp. 2873–2911. URL <http://www.jstor.org/stable/2666834>.
- [4] Siquig, R., “Impact of Icing on Unmanned Aerial Vehicle (UAV) Operations,” 1990.
- [5] Szilder, K., and McIlwain, S., “In-Flight Icing of UAVs - The Influence of Reynolds Number on the Ice Accretion Process,” *SAE Technical Paper Series*, 2011. <https://doi.org/10.4271/2011-01-2572>.
- [6] Fajt, N., Hann, R., and Lutz, T., “The Influence of Meteorological Conditions on the Icing Performance Penalties on a UAV Airfoil,” *8th European Conference for Aeronautics and Space Sciences (EUCASS)*, , No. July, 2019.
- [7] Hann, R., Hearst, R. J., Sætran, L. R., and Bracchi, T., “Experimental and Numerical Icing Penalties of an S826 Airfoil at Low Reynolds Numbers,” *Aerospace*, Vol. 7, No. 4, 2020, p. 46. <https://doi.org/10.3390/aerospace7040046>.
- [8] Williams, N., Benmeddour, A., Brian, G., and Ol, M., “The effect of icing on small unmanned aircraft low Reynolds number airfoils,” 2017.
- [9] Liu, Y., Li, L., Ning, Z., Tian, W., and Hu, H., “Experimental investigation on the dynamic icing process over a rotating propeller model,” *Journal of Propulsion and Power*, Vol. 34, No. 4, 2018, pp. 933–946. <https://doi.org/10.2514/1.B36748>.
- [10] Liu, Y., Li, L., Chen, W., Tian, W., and Hu, H., “An experimental study on the aerodynamic performance degradation of a UAS propeller model induced by ice accretion process,” *Experimental Thermal and Fluid Science*, Vol. 102, No. November 2018, 2019, pp. 101–112. <https://doi.org/10.1016/j.expthermflusci.2018.11.008>, URL <https://doi.org/10.1016/j.expthermflusci.2018.11.008>.

- [11] Hann, R., Enache, A., Nielsen, M. C., Stovner, B. N., van Beeck, J., Johansen, T. A., and Borup, K. T., “Experimental Heat Loads for Electrothermal Anti-Icing and De-Icing on UAVs,” *Aerospace*, Vol. 8, No. 3, 2021, p. 83. <https://doi.org/10.3390/aerospace8030083>.
- [12] Hann, R., Borup, K., Zolich, A., Sorensen, K., Vestad, H., Steinert, M., and Johansen, T., “Experimental Investigations of an Icing Protection System for UAVs,” *SAE Technical Paper Series*, 2019. <https://doi.org/10.4271/2019-01-2038>.
- [13] Hann, R., and Johansen, T. A., “Unsettled Topics in Unmanned Aerial Vehicle Icing,” *SAE Edge Report*, 2020. <https://doi.org/https://doi.org/10.4271/EPR2020008>, URL <https://doi.org/10.4271/EPR2020008>.
- [14] Papadakis, M., Aeronautics, U. S. N., Administration, S., Center, L. R., and (U.S.), F. A. A. T. C., “An Experimental Method for Measuring Water Droplet Impingement Efficiency on Two- and Three-dimensional Bodies,” *NASA Contractor Report 4257 DOT/FAA/CT-87/22*, 1989. URL <https://books.google.no/books?id=siwF3m7qRx0C>.
- [15] Pastor-Barsi, C., and Arrington, A., “Aero-Thermal Calibration of the NASA Glenn Icing Research Tunnel (2012 Test),” *4th AIAA Atmospheric and Space Environments Conference*, 2012. <https://doi.org/10.2514/6.2012-2934>.
- [16] Hann, R., and Müller, N., “Icing Validation Database,” , 2020. <https://doi.org/10.18710/5XYALW>.
- [17] Liu, Y., Li, L., Ning, Z., Tian, W., and Hu, H., “An experimental study on the transient ice accretion process over the blade surfaces of a rotating UAS propeller,” *AIAA SciTech Forum - 55th AIAA Aerospace Sciences Meeting*, , No. January, 2017. <https://doi.org/10.2514/6.2017-0727>.
- [18] Han, Y., Palacios, J. L., and Smith, E. C., “An experimental correlation between rotor test and wind tunnel ice shapes on NACA 0012 airfoils,” *SAE Technical Papers*, 2011. <https://doi.org/10.4271/2011-38-0092>.
- [19] McCormick, B., *Aerodynamics, Aeronautics, and Flight Mechanics*, Vol. 2nd Edition, Wiley, 1995.
- [20] ANSYS Inc., “ANSYS FENSAP-ICE User Manual, Release 20.1,” , 2020.
- [21] Beaugendre, H., Morency, F., and Habashi, W. G., “FENSAP-ICE’s Three-Dimensional In-Flight Ice Accretion Module: ICE3D,” *Journal of Aircraft*, Vol. 40, No. 2, 2003, pp. 239–247. <https://doi.org/10.2514/2.3113>, URL <https://doi.org/10.2514/2.3113>.
- [22] Isik, O., David, S., Guido S., B., and Chen, J., “Multi-Shot Icing Simulations with Automatic Re-Meshing,” *SAE Technical Paper*, Vol. 2019-01-1956, 2019.
- [23] Deters, R., “Performance and Slipstream Characteristics of small-scale Propellers at low Reynolds Numbers,” Ph.D. thesis, 2014.
- [24] Drela, M., “XFOIL: An Analysis and Design System for Low Reynolds Number Airfoils.” *MIT Dept. of Aeronautics and Astronautics*, 1989.
- [25] Airfoil Tools, “CLARK Y AIRFOIL - CLARK Y airfoil Seen on 2020-10-09,” , 2020. URL <http://airfoiltools.com/airfoil/details?airfoil=clarky-il>, <http://airfoiltools.com/airfoil/details?airfoil=clarky-il>.
- [26] Dassault Systèmes, “CATIA Documentation Version 5 Release 19,” 2008.
- [27] Maritime Robotics, “PX-31 Unmanned Aircraft System [UAS] Seen on 9.10.2020,” , 2020. <https://pdf.aeroexpo.online/pdf/maritime-robotics/px-31-brochure/181323-12497.html>.
- [28] Federal Aviation Administration (FAA), “Part I – Atmospheric Icing Conditions,” *Title 14 CFR Part 25 Appendix C, Doc. No. 4080, 29 FR 17955, Amdt. 25-140, 79 FR 65528*, 2014.
- [29] Fajt, N., Hann, R., and T., L., “The Influence of Meteorological Conditions on the Icing Performance Penalties on a UAV Airfoil,” *8th European Conference for Aeronautics and Aerospace Sciences (EUCASS)*, 2019.
- [30] Rüdiger, S., *CFD-Modellierung: Grundlagen und Anwendungen bei Strömungsprozessen*, Springer Vieweg, 2013.
- [31] Hann, R., “Atmospheric Ice Accretions, Aerodynamic Icing Penalties, and Ice Protection Systems on Unmanned Aerial Vehicles,” Ph.D. thesis, Norwegian University of Science and Technology, 2020.
- [32] NATO RTO Technical Report 38, “Ice Accretion Simulation Evaluation Test,” *RTO-TR-038 AC/323(AVT-006)TP/26*, 2001.